Journal of Power Sources 247 (2014) 178–183

Contents lists available at ScienceDirect

Journal of Power Sources

journal homepage: www.elsevier.com/locate/jpowsour

Highly loaded SnO_2/mesoporous carbon nanohybrid with well-improved lithium storage capability

Lian Chen [a], Ping Wu [a, *], Hui Wang [a], Ya Ye [a], Bin Xu [b], Gaoping Cao [b], Yiming Zhou [a, *], Tianhong Lu [a], Yusheng Yang [b]

[a] Jiangsu Key Laboratory of New Power Batteries, Jiangsu Collaborative Innovation Center of Biomedical Functional Materials, School of Chemistry and Materials Science, Nanjing Normal University, Nanjing 210023, PR China
[b] Research Institute of Chemical Defense, Beijing 100191, PR China

HIGHLIGHTS

- Self-made mesoporous carbon (MC) as a novel supporting matrix for SnO_2 anode.
- High and uniform loading of SnO_2 on MC matrix via a facile chemical solution route.
- Markedly improved lithium storage capability by virtue of its structure superiority.

GRAPHICAL ABSTRACT

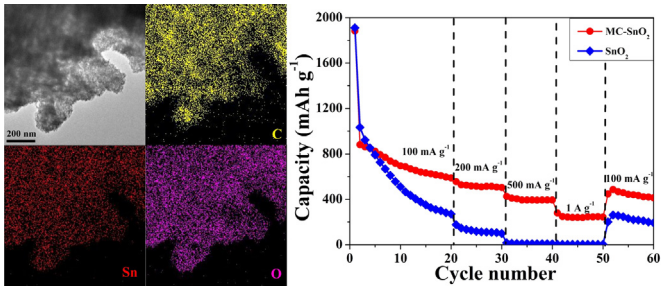

ARTICLE INFO

Article history:
Received 30 May 2013
Received in revised form
13 August 2013
Accepted 17 August 2013
Available online 3 September 2013

Keywords:
Tin oxide
Mesoporous carbon
Nanohybrid
Anode
Li-ion batteries

ABSTRACT

This paper reports the synthesis of highly loaded SnO_2/mesoporous carbon (MC) nanohybrid through a facile chemical solution process and subsequent annealing methodology, by using a novel three-dimensional (3D) MC as a buffering and conducting matrix. Owing to its unique structural characteristics, the MC–SnO_2 nanohybrid anode exhibits markedly improved cycling stability and rate capability compared to pure SnO_2 nanoparticles, facilitating its application in advanced Li-ion batteries (LIBs) with long cycle life and high power density.

1. Introduction

Expansion of lithium ion technology into consumer electronics, electric vehicles and energy storage devices requires the development of advanced battery systems with low cost, long life, high energy and power densities, which are intrinsically controlled by the electrode materials [1]. Among them, tin-based materials especially tin dioxide (SnO_2) have been considered as promising anodes for advanced Li-ion batteries (LIBs) due to their much higher theoretical capacities than conventional graphite (372 mAh g^{-1}) [2]. Unfortunately, the commercialization process of SnO_2 has been frustrated primarily by its huge volume change (~300%) during the charge–discharge process, which leads to serious pulverization and fast capacity fading [3].

* Corresponding authors. Tel.: +86 25 85891651; fax: +86 25 83243286.
E-mail addresses: zjuwuping@njnu.edu.cn (P. Wu), zhouyiming@njnu.edu.cn (Y. Zhou).

0378-7753/$ – see front matter © 2013 Elsevier B.V. All rights reserved.
http://dx.doi.org/10.1016/j.jpowsour.2013.08.059

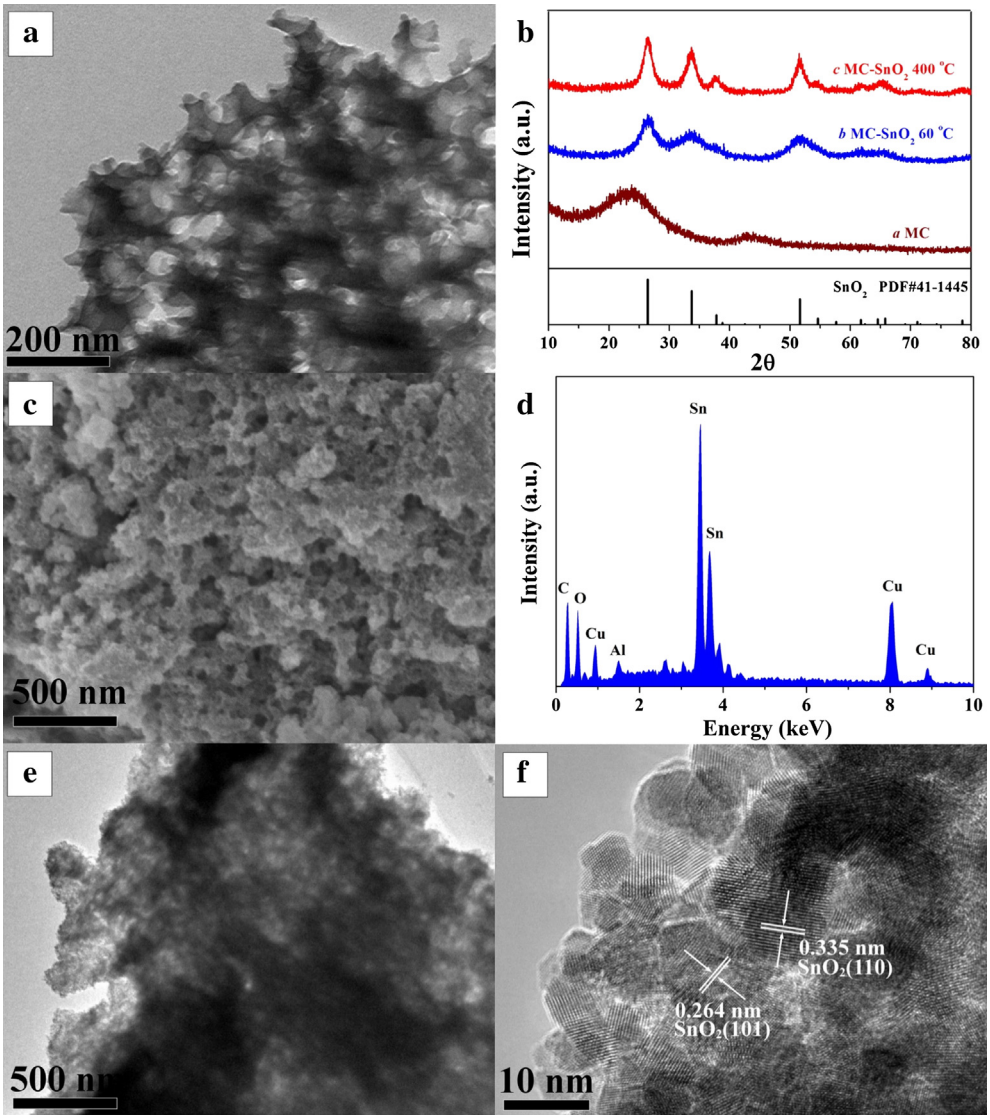

Fig. 1. (a) TEM image of MC matrix; (b) XRD patterns of MC matrix (curve *a*), MC–SnO_2 nanohybrid before (curve *b*) and after (curve *c*) the annealing process; (c–f) Morphological, structural and compositional characterizations of MC–SnO_2 nanohybrid: (c) FESEM image; (d) EDX spectrum; (e) TEM image; (f) HRTEM image.

Various SnO_2 nanostructures [3–6], such as nanotubes [4], nanosheets [5], hollow nanospheres [6], and so forth, have been designed to accommodate the volume changes owing to their large surface area and pore volume. However, the stability of single-component nanostructured anodes remains a significant challenge [7]. Their structural collapse also causes particle agglomeration, pulverization and capacity fading upon cycling. In addition, the low intrinsic electronic conductivity of pure SnO_2 hinders fast charge transport, resulting in poor rate capability [8].

To address the aforementioned issues, much attention has been paid to the fabrication of SnO_2-based nanohybrids by introducing appropriate buffering/conducting matrixes [8–16]. Among various matrixes, carbon materials, such as amorphous carbon [11,12], carbon nanotubes (CNTs) [13,14], and graphene [15,16], have been considered as the most promising choices owing to their excellent buffering effect and high electronic conductivity. Compared to zero-dimensional (0D), 1D and 2D carbon matrixes, three-dimensional (3D) porous carbon scaffolds materials possess higher mechanical stability, charge transport capability, host capability, and so forth [17–20]. Therefore, the nanohybrids of SnO_2 and 3D porous carbon matrix are expected to exhibit well-improved cycling stability and rate capability. For example, 3D ordered mesoporous carbon scaffolds derived from silica (SBA-15) have been demonstrated to be promising matrixes for SnO_2 anodes with significantly improved lithium storage performance [21–24]. However, the synthetic routes are tedious and complex, and the template-removing process using corrosive HF is environmentally unfriendly, which hinders the mass production and practical application of SnO_2 anodes. It's highly desirable to obtain such SnO_2-based anodes through more facile, scalable, and environmentally benign processes.

Herein, we report the synthesis of SnO_2-based nanohybrid through a facile chemical solution process and subsequent annealing methodology, by using nano-$CaCO_3$-templated 3D mesoporous carbon (MC) as a buffering and conducting matrix. When evaluated as an anode for LIBs, the MC–SnO_2 nanohybrid exhibits markedly improved cycling stability and rate capability owing to its unique structural characteristics.

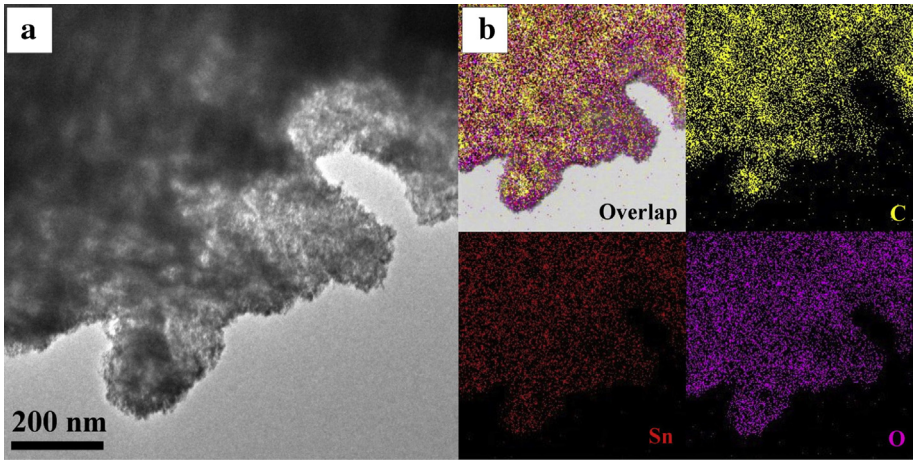

Fig. 2. TEM–EDX elemental mappings of MC–SnO_2 nanohybrid: (a) TEM image; (b) EDX elemental mapping of C (yellow), Sn (red), O (purple), and their overlap. (For interpretation of the references to color in this figure legend, the reader is referred to the web version of this article.)

2. Experimental section

2.1. Synthesis of MC–SnO_2 nanohybrid

All the chemicals were analytical grade. MC matrix was prepared through a nano-$CaCO_3$-templated approach according to our previous report [25]. The pristine MC matrix was pretreated by refluxing in HNO_3 (65 wt%) solution for 5 h, followed by washing with deionized water and drying at 60 °C before use. MC–SnO_2 nanohybrid was prepared through a chemical solution process and subsequent annealing approach. Typically, 100 mg pretreated MC was dispersed in 20 mL deionized water, and then 0.25 mL HCl (38 wt%), 0.5 g $SnCl_2 \cdot H_2O$ and 0.25 g urea were added. The mixture was refluxed at 60 °C for 6 h under stirring. After the reaction was finished, the resulting solid products were centrifuged, washed with deionized water and dried at 60 °C in air. Finally, the products were kept in a tube furnace at 400 °C for 2 h under nitrogen at a ramping rate of 5 °C min^{-1}. For comparison, pure SnO_2 nanoparticles were synthesized by the same method but without adding MC matrix.

2.2. Characterization

The morphology, composition, and structure of the samples were characterized by transmission electron microscopy (TEM, Hitachi H-7650, 120 kV), high-resolution transmission electron microscopy (HRTEM, JEOL JEM-2010F, 200 kV) equipped with energy-dispersive X-ray spectrometer (EDX, Thermo Fisher Scientific, NORAN System 7), and field emission scanning electron microscopy (FESEM, Hitachi S-4800) equipped with EDX (Horiba,

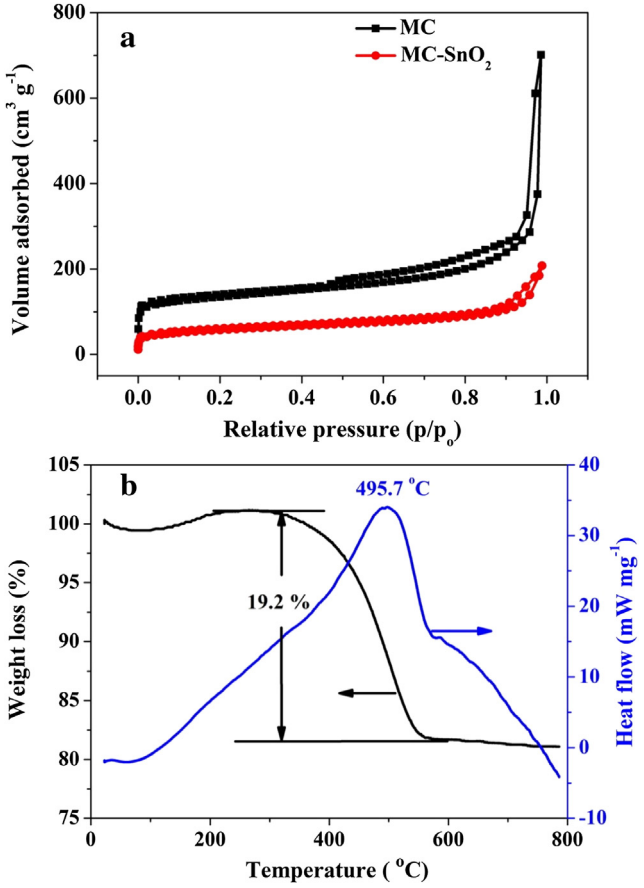

Fig. 3. (a) Nitrogen adsorption/desorption isotherms of MC matrix and MC–SnO_2 nanohybrid at 77 K; (b) DSC–DTA analysis of MC–SnO_2 nanohybrid.

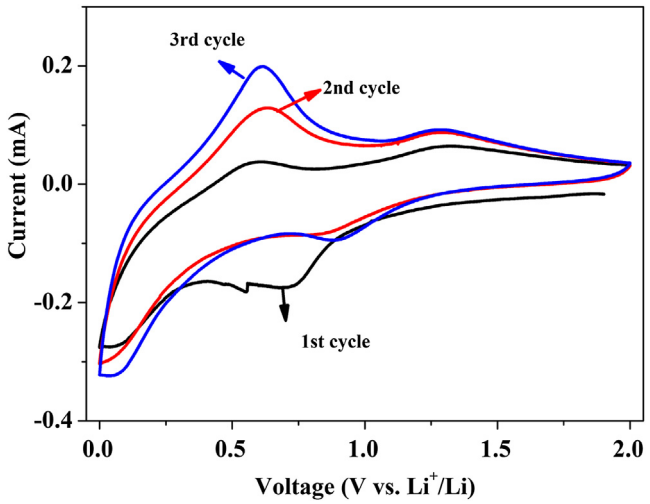

Fig. 4. CV curves of MC–SnO_2 nanohybrid in the initial three cycles in the potential range of 0.0–2.0 V at a scan rate of 0.1 mV s^{-1}.

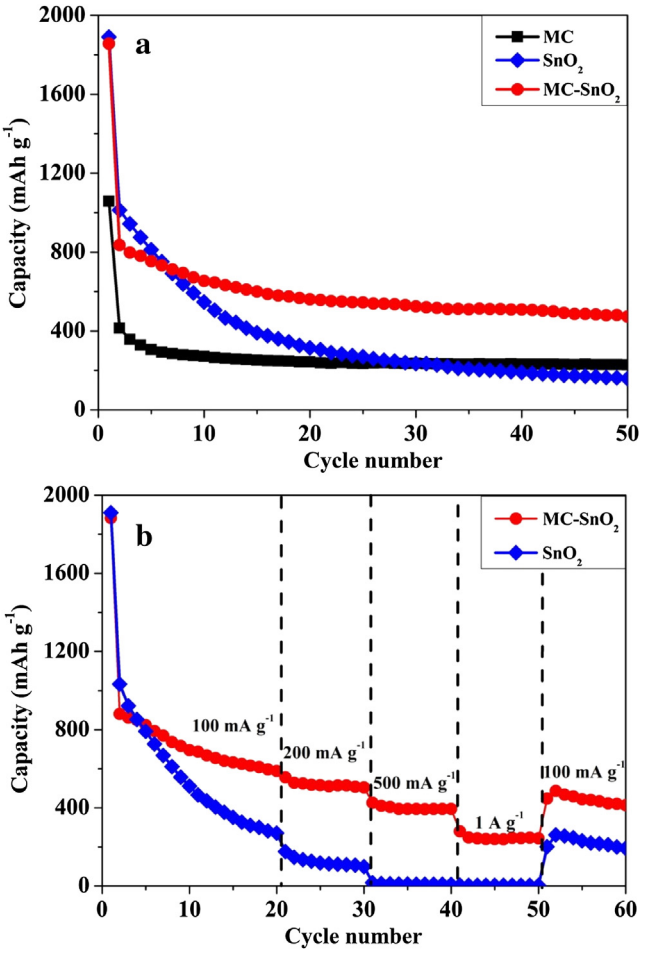

Fig. 5. (a) Cycling performance and (b) rate capability of MC matrix, pure SnO_2 nanoparticles, and MC–SnO_2 nanohybrid.

7593-H). X-ray powder diffraction (XRD) measurements were performed with Model D/max-rC diffractometer using Cu-Kα radiation ($\lambda = 0.15406$ nm) and operating at 45 kV and 100 mA. The zeta potential measurements were carried out on a Malvern Zetasizer Nano ZS90 analyzer at room temperature. The Brunauer–Emmett–Teller (BET) specific surface area and pore size distribution were measured at 77 K using a Micromeritics ASAP 2050 system. The differential scanning calorimetry and thermogravimetric analysis (DSC–TGA) was performed on a Perkin Elmer Diamond instrument in air at a ramping rate of 5 °C min^{-1}.

2.3. Electrochemical measurements of MC–SnO_2 nanohybrid

The electrochemical performance of the composite electrode was measured using coin-type cells assembled in an argon-filled glove box. The working electrodes were prepared by pasting slurries onto Cu foam current collector, and dried at 120 °C for 12 h under vacuum before testing. The slurry was made by mixing active material (MC–SnO_2 nanohybrid), conductive materials (Super P carbon black), and binder (polyvinylidene difluoride, PVDF) in a weight ratio of 80:10:10 in N-methyl-2-pyrrolidone (NMP). MC matrix in MC–SnO_2 nanohybrid was considered as part of active material when calculating the specific capacity of nanohybrid anode. Lithium foil was used as the counter electrode, 1 mol L^{-1} $LiPF_6$ in ethylene carbonate (EC)/dimethyl carbonate (DMC) (1:1 in volume ratio) as the electrolyte and Celgard 2400 film as separator in the coin cell. Galvanostatic cycling tests of the assembled cells were carried out on a Land CT2001A system (Wuhan, China) in the potential range of 0.01–2 V at various current densities. Cyclic voltammetry (CV) measurements were recorded on a CHI 660B electrochemical analyzer (Shanghai CH Instrument Company, China) in the potential range of 0.0–2.0 V at a scan rate of 0.1 mV s^{-1}. The voltages mentioned herein were referred to Li^+/Li redox couple.

3. Results and discussion

Recently, 3D templated interconnected networks such as copper [26], nickel [27], and carbon [21–24] have shown great potential as buffering/conducting matrixes for electrode materials in LIBs. Herein, 3D MC interconnected network has been demonstrated as an advanced supporting matrix for SnO_2 anodes in LIBs. The methodology for MC–SnO_2 nanohybrid presented here has several advantages compared to the previous reported approaches using silica-derived MC as matrixes [21–24]. First, the preparation of MC matrix using nano-$CaCO_3$ as a template is facile, scalable, and environmentally friendly. Second, the nano-$CaCO_3$-templated MC matrix possesses large homogeneous mesopores (~40 nm, Fig. 1a) and thus enhanced host capabilities, which is beneficial for the high and uniform loading of SnO_2. Third, SnO_2 nanocrystals can be filled

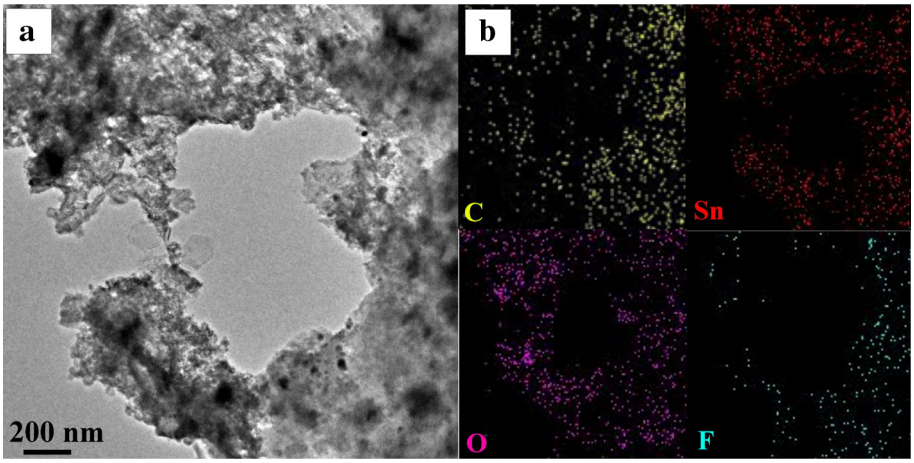

Fig. 6. TEM–EDX elemental mappings of MC–SnO_2 nanohybrid in a fully de-lithiated state after 20 cycles: (a) TEM image; (b) EDX elemental mappings of C, Sn, O, and F, respectively.

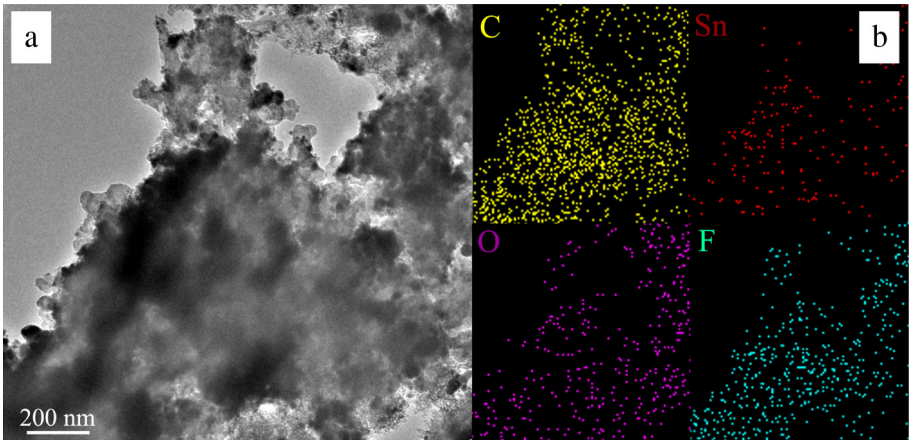

Fig. 7. TEM–EDX elemental mappings of pure SnO_2 nanoparticles in a fully de-lithiated state after 20 cycles: (a) TEM image; (b) EDX elemental mappings of C, Sn, O, and F, respectively.

into the mesopores of MC matrix *via* a facile chemical solution process. Therefore, the methodology demonstrated here facilitates the mass production and practical application of MC-SnO_2 nanohybrid.

The crystalline structure of the samples was characterized by XRD (Fig. 1b). As observed, the broad peaks located at about 23° and 43° in curve *a* correspond to MC with poor crystallinity. After the deposition of SnO_2, the observed crystalline phase from curve *b* and *c* can be assigned to tetragonal SnO_2 (JCPDS: 41-1445). The calculated average crystallite size of SnO_2 increases slightly from ~3 to 5 nm after the annealing process. The FESEM image (Fig. 1c) shows that the MC–SnO_2 nanohybrid retains the 3D porous structure, but has a much rougher surface than MC matrix. Fig. 1d gives the EDX spectrum of the MC–SnO_2 nanohybrid. As observed, the strong peaks for C, Sn, and O elements are expected from MC matrix and SnO_2 nanoparticles, respectively, while the Cu and Al peaks come from the sample stage used in the FESEM measurements.

Fig. 1e and f display the TEM and HRTEM images of MC–SnO_2 nanohybrid. As observed from the TEM image, numerous SnO_2 nanoparticles are uniformly distributed on the concave–convex surface of MC matrix. After acid treatment, the zeta potential of MC matrix changes from −1.4 to −19.7 mV, since the introduction of carboxyl groups on its pore walls. The negatively charged carboxyl groups can serve as efficient adsorption sites for Sn^{2+} ions, and the subsequently formed SnO_2 nuclei are deposited uniformly on the matrix surface, yielding MC–SnO_2 nanohybrid. Moreover, the HRTEM image displays two kinds of lattice fringes with the lattice spacings of about 0.264 and 0.335 nm, corresponding to the (101) and (110) planes of SnO_2 nanoparticles, respectively.

TEM–EDX elemental mapping analysis was used to further characterize the elemental distribution of the products. Fig. 2 displays a typical TEM image taken from the edge part of the MC-SnO_2 nanohybrid, along with the corresponding elemental maps of C, Sn, O, and their overlap. As observed, Sn and O signals are uniformly distributed over the chosen region, which is almost consistent with C signal. The elemental mapping analysis confirms the uniform distribution of SnO_2 nanoparticles within MC matrix.

To obtain further insight into their 3D porous structure, the surface area of the MC matrix and MC-SnO_2 nanohybrid was characterized by nitrogen adsorption–desorption isotherms at 77 K in Fig. 3a. It is found that the MC matrix has a BET surface area of 435.1 $m^2\ g^{-1}$ with a pore volume of 0.835 $cm^3\ g^{-1}$. After the loading of SnO_2, the values decrease to 193.7 $m^2\ g^{-1}$ and 0.251 $cm^3\ g^{-1}$, demonstrating the moderate rather than complete filling of SnO_2 into the carbon mesopores. Moreover, DSC–TGA was performed to determine the SnO_2 content presented in the MC–SnO_2 nanohybrid. As observed from Fig. 3b, the weight loss between 200 and 600 °C (19.2 wt%) accompanied with an exothermic peak at 495.7 °C can be attributed mainly to the removal of MC matrix. Thus, the SnO_2 content of MC–SnO_2 nanohybrid is determined to be as high as 80.8 wt%. The moderate pore-filling of SnO_2 favors enhanced cycling stability, whereas the high loading of SnO_2 is beneficial for increased specific capacities. Therefore, the MC–SnO_2 nanohybrid demonstrating here is expected to exhibit improved lithium storage performance.

The as-synthesized MC–SnO_2 nanohybrid was used as a potential anode for LIBs. Fig. 4 shows the initial three CV curves of nanohybrid anode in the potential range of 0.0–2.0 V at a scan rate of 0.1 mV s^{-1}. As observed, the profiles of these CV curves are characteristic of SnO_2-based anodes [9–16]. The lithiation/delithiation mechanism of SnO_2 anodes is a conversion followed by alloying/de-alloying reactions:

$$SnO_2 + 4Li^+ + 4e^- \rightarrow Sn + 2Li_2O \quad (1)$$

$$Sn + xLi^+ + xe^- \leftrightarrow Li_xSn\ (0 \le x \le 4.4)\,. \quad (2)$$

In the first cycle, the broad cathodic peak at about 0.73 V can be attributed to the formation of solid electrolyte interface (SEI) layer, and reduction of SnO_2 to Sn and Li_2O described by equation (1). These processes are generally believed to be irreversible, leading to large initial irreversible capacity. Herein, this cathodic peak shifts to a higher voltage (around 0.9 V) rather than disappear entirely in subsequent cycles, and the peak intensity is significantly reduced, which could be explained by the partial reversibility of the reduction reaction described by equation (1) [5,28]. In addition, the characteristic pair (cathodic, anodic) of current peaks located at (0.06, 0.6 V) could be ascribed to the alloying and de-alloying processes described by equation (2), which is believed to be highly reversible. It could be noticed that the intensity of both cathodic and anodic peaks gradually increases in the second and third cycles, demonstrating the existence of possible activating processes in the nanohybrid anode [11,28,29].

Fig. 5a displays the discharge capacities as a function of cycle number for the MC–SnO_2 nanohybrid anode at a current density of 100 mA g^{-1} in the potential range of 0.01–2 V. For comparison, cycling performance of MC matrix and pure SnO_2 nanoparticles were also investigated under the same conditions. As observed, the initial discharge capacities of pure SnO_2 nanoparticles, MC–SnO_2 nanohybrid, and MC matrix are 1890.5, 1855.7, and 1057.5 mAh g^{-1},

respectively, due to the gradual decrease of SnO_2 content. The discharge capacities of MC–SnO_2 nanohybrid experience a slowly fading process and maintain at 473.1 mAh g^{-1} after 50 cycles with a retention of 56.6% comparing with the first reversible capacity. On contrast, the pure SnO_2 experiences rapid capacity fading upon cycling. After 50 cycles, the discharge capacity is only 157.9 mAh g^{-1}, which is much lower than that of MC–SnO_2 nanohybrid.

Moreover, the rate capability of MC–SnO_2 nanohybrid was examined in comparison with pure SnO_2 nanoparticles at various current densities from 100 to 1000 mA g^{-1} (Fig. 5b). As observed, the MC–SnO_2 nanohybrid delivers a discharge capacity of 588.5 mAh g^{-1} at a current density of 100 mA g^{-1} after 20 cycles. This value decreases to 516.0 mAh g^{-1} (200 mA g^{-1}), 394.0 mAh g^{-1} (500 mA g^{-1}), 240.0 mAh g^{-1} (1000 mA g^{-1}), and finally returns to 443.9 mAh g^{-1} at 100 mA g^{-1}. In sharp contrast, the discharge capacities of pure SnO_2 decrease rapidly with the increase of current densities. These results demonstrate that the MC–SnO_2 nanohybrid possesses markedly improved rate capability, making it a promising anode for LIBs with high power densities.

Fig. 6 shows the TEM–EDX elemental mappings of MC–SnO_2 nanohybrid in a fully de-lithiated state after 20 cycles. As observed from the TEM image, the 3D porous structure of MC–SnO_2 nanohybrid is well preserved, and the agglomeration and pulverization of SnO_2 nanoparticles can be effectively restrained. Moreover, the elemental mapping images indicate the tin component is still evenly distributed within the MC matrix. In addition, the F signal comes from the SEI layer, which consists of the decomposition products of $LiPF_6$-based electrolytes. In sharp contrast, the pure SnO_2 nanoparticles become larger and agglomerated after cycling (Fig. 7a), and the elemental mappings also demonstrate the nonuniform distribution of Sn signal within the chosen region (Fig. 7b). These results confirm the structural stability of the SnO_2 anodes has been significantly enhanced by introducing MC matrix, which can further explain the huge differences in lithium storage capabilities of MC–SnO_2 nanohybrid and pure SnO_2 nanoparticles.

4. Conclusions

In summary, we have synthesized MC–SnO_2 nanohybrid with high SnO_2 content (80.8 wt%) through a facile chemical solution process and subsequent annealing methodology by using MC as a novel buffering and supporting matrix. Compared to pure SnO_2 nanoparticles, the MC–SnO_2 nanohybrid exhibits markedly improved cycling stability and rate capability, which makes it a promising anode for long-life and high-power LIBs. For example, a high capacity of 473.1 mAh g^{-1} from MC–SnO_2 nanohybrid can be retained after 50 cycles, which is much higher than that of pure SnO_2 nanoparticles (157.9 mAh g^{-1}). The improved lithium storage performance can be ascribed to the MC matrix with excellent structural stability and high charge transport capability, which could be applied to other anode/cathode systems for their enhanced performance.

Acknowledgments

The authors appreciate the financial supports from Industry-Academia Cooperation Innovation Fund Project of Jiangsu Province (BY2012001), Natural Science Foundation of Jiangsu Higher Education Institutions of China (13KJB150026), a project funded by the Priority Academic Program Development of Jiangsu Higher Education Institutions, and the Priming Scientific Research Foundation for Advanced Talents in Nanjing Normal University (2013103XGQ0008).

References

[1] V. Etacheri, R. Marom, R. Elazari, G. Salitra, D. Aurbach, Energy Environ. Sci. 4 (2011) 3243–3262.
[2] Y. Idota, T. Kubota, A. Matsufuji, Y. Maekawa, T. Miyasaka, Science 276 (1997) 1395–1397.
[3] J.S. Chen, X.W. Lou, Small 9 (2013) 1877–1893.
[4] X. Xu, J. Liang, H. Zhou, D. Lv, F. Liang, Z. Yang, S. Ding, D. Yu, J. Mater. Chem. A 1 (2013) 2995–2998.
[5] C. Wang, G. Du, K. Stahl, H. Huang, Y. Zhong, J. Jiang, J. Phys. Chem. C 116 (2012) 4000–4011.
[6] S. Ding, X.W. Lou, Nanoscale 3 (2011) 3586–3588.
[7] A.L.M. Reddy, S.R. Gowda, M.M. Shaijumon, P.M. Ajayan, Adv. Mater. 24 (2012) 5045–5064.
[8] N.S. Choi, Y. Yao, Y. Cui, J. Cho, J. Mater. Chem. 21 (2011) 9825–9840.
[9] Z. Yang, G. Du, Q. Meng, Z. Guo, X. Yu, Z. Chen, T. Guo, R. Zeng, RSC Adv. 1 (2011) 1834–1840.
[10] Z. Du, S. Zhang, T. Jiang, X. Wu, L. Zhang, H. Fang, J. Power Sources 219 (2012) 199–203.
[11] P. Wu, N. Du, H. Zhang, J. Yu, Y. Qi, D. Yang, Nanoscale 3 (2011) 746–750.
[12] P. Wu, N. Du, H. Zhang, C. Zhai, D. Yang, ACS Appl. Mater. Interfaces 3 (2011) 1946–1952.
[13] Y. Zhao, J. Li, Y. Ding, L. Guan, RSC Adv. 1 (2011) 852–856.
[14] P. Wu, N. Du, H. Zhang, J. Yu, D. Yang, J. Phys. Chem. C 114 (2010) 22535–22538.
[15] X. Wang, X. Zhou, K. Yao, J. Zhang, Z. Liu, Carbon 49 (2011) 133–139.
[16] L. Wang, D. Wang, H.Z. Dong, F. Zhang, J. Jin, Nano Lett. 13 (2013) 1711–1716.
[17] H. Nishihara, T. Kyotani, Adv. Mater. 24 (2012) 4473–4498.
[18] L. Shen, X. Zhang, E. Uchaker, C. Yuan, G. Cao, Adv. Energy Mater. 2 (2012) 691–698.
[19] B. Xu, L. Shi, X. Guo, L. Peng, Z. Wang, S. Chen, G. Cao, F. Wu, Y. Yang, Electrochim. Acta 56 (2011) 6464–6468.
[20] L. Chen, P. Wu, K. Xie, J. Li, B. Xu, G. Cao, Y. Chen, Y. Tang, Y. Zhou, T. Lu, Y. Yang, Electrochim. Acta 92 (2013) 433–437.
[21] J. Fan, T. Wang, C. Yu, B. Tu, Z. Jiang, D. Zhao, Adv. Mater. 16 (2004) 1432–1436.
[22] H. Qiao, J. Li, J. Fu, D. Kumar, Q. Wei, Y. Cai, F. Huang, ACS Appl. Mater. Interfaces 3 (2011) 3704–3708.
[23] F. Han, W. Li, M. Li, A. Lu, J. Mater. Chem. 22 (2012) 9645–9651.
[24] S. Ding, Z. Wang, S. Madhavi, X.W. Lou, J. Mater. Chem. 21 (2011) 13860–13864.
[25] B. Xu, L. Peng, G. Wang, G. Cao, F. Wu, Carbon 48 (2010) 2377–2380.
[26] J. Wang, N. Du, Z. Song, H. Wu, H. Zhang, D. Yang, J. Power Sources 229 (2013) 185–189.
[27] H. Zhang, X. Yu, P. Braun, Nat. Nanotechnol. 38 (2011) 1–5.
[28] S. Ding, D. Zhang, H.B. Wu, Z. Zhang, X.W. Lou, Nanoscale 4 (2012) 3651–3654.
[29] J.S. Chen, Y.L. Cheah, Y.T. Chen, N. Jayaprakash, S. Madhavi, Y.H. Yang, X.W. Lou, J. Phys. Chem. C 113 (2009) 20504–20508.